

Thomas Blesgen

# On rotation deformation zones for finite-strain Cosserat plasticity

Received: October 4, 2014. Revised: January 1, 2015.

**Abstract** In this article, a numerical solution method for the finite-strain rate-independent Cosserat theory of crystal-plasticity is developed. Based on a time-incremental minimization problem of the mechanical energy, a limited-memory Broyden-Fletcher-Goldfarb quasi-Newton method applied to a finite-difference discretization is proposed. First benchmark tests study the convergence to an analytic solution. Further simulations focus on the investigation of rotation localization zones, the bending of a rod and a torsion experiment.

**Keywords** Cosserat theory · Plasticity · Quasi-Newton methods

## 1 Introduction

The Cosserat model, introduced in 1909 by the Cosserat brothers, [13], is a general theory of continuum mechanics that accounts for independent rotations. For decades, only a few publications dealt with the Cosserat theory. Then, starting in the late 1950ies, there came a Renaissance of the model, leading to the development of the linear Cosserat theory, see [33, 21, 2, 62, 44], and [61] for further references. Also, the pioneering work [19] introduced a new, direct approach, resulting in applications for shells, beams, and plates, see, e.g., [69, 32, 15, 57]. Since then, the Cosserat model has been successfully applied to a wide range of different problems, like directed fluids, liquid crystals, powders, or granular materials, see [4, 22, 25, 66, 11, 16, 35, 64, 39] and others. Recent reviews on the Cosserat theory can be found in the survey articles [18, 42, 5, 28, 47, 56].

From its construction, the Cosserat model is a gradient model. In that, contrary to other established models in elasto-plasticity like [36, 43, 58, 59], it automatically induces a length scale, with the effect that the localization zones always have a finite width.

The focus of this article lies in the development of a new algorithm for the finite-strain Cosserat theory of crystal-plasticity. Among the earlier numerical studies of Cosserat models, the articles [9, 29, 30, 38, 48, 49, 53, 68] are mentioned here which investigate the infinitesimal elasto-plastic Cosserat model. In [41, 31, 37], a numerical approach for the finite-strain case is introduced. Therein, fictitious, e.g. theoretically hypothesized intermediate material configurations are postulated to get around the costly computation of the micro-rotations. However, these intermediate configurations need not exist, see [46, 55]. The algorithm developed here constitutes an alternate approach. The computed micro-rotations also yield new insights on rotation localization phenomena in deformed solids.

The article is organized in the following way. In Section 2, the finite-strain Cosserat model and the time-incremental minimization ansatz of the mechanical energy functional are recalled. The latter puts the problem in a framework suitable to the calculus of variations. Section 3 develops a quasi-Newton algorithm for the numerical computation of the minimizers which is based on a finite difference scheme. The final section is

---

T. Blesgen  
Department of Mathematics, Bingen University of Applied Sciences, Berlinstraße 109, D-55411 Bingen, Germany  
Tel.: +49-6721-409252  
Fax: +49-6721-409158  
E-mail: t.blesgen@fh-bingen.de

devoted to numerical simulations. The article ends with a discussion of the results. To simplify reading, a complete list of symbols is provided in the appendix.

## 2 The Cosserat theory within the framework of large-strain rate-independent crystal-plasticity

In the Cosserat theory of rate-independent large-strain crystal-plasticity, the evolution of a plastically deformed solid in the absence of surface tractions and surface couples is governed by the time-discrete minimization problem, [7],

$$\begin{aligned} \mathcal{E}(\varphi, R_e, \gamma) := & \int_{\Omega} \left[ W_{st}(R_e^t D\varphi F_p(\gamma)^{-1}) + W_c(K_e) + \rho \left( \sum_{a=1}^{I_p} |\gamma_a - \gamma_a^0| \right)^2 \right. \\ & \left. - f_{\text{ext}} \cdot \varphi - M_{\text{ext}} : R_e + \sum_{a=1}^{I_p} |\gamma_a - \gamma_a^0| \left( \sigma_Y - 2\rho \sum_{a=1}^{I_p} \kappa_a^0 \right) \right] dx \rightarrow \min \end{aligned} \quad (1)$$

subject to the initial and Dirichlet boundary conditions

$$\begin{aligned} \varphi(x, 0) &= x, \quad \kappa(\cdot, 0) = \kappa^0 & \text{in } \Omega, \\ \varphi &= g_D, \quad R_e = R_D & \text{on } \partial\Omega. \end{aligned} \quad (2)$$

Either,  $R_D$  is fixed Dirichlet boundary data or is defined by

$$R_D := \text{polar}(Dg_D F_p^{-1}). \quad (3)$$

Here, if  $A = U\Sigma V^t$  is the singular value decomposition (SVD) of a real tensor  $A$ , then the polar decomposition is given by

$$\text{polar}(A) := UV^t. \quad (4)$$

In deriving (1), Lagrange coordinates are introduced with  $\Omega \subset \mathbb{R}^d$  denoting the undeformed reference configuration of the material. The deformation of  $\Omega$  is controlled by  $\varphi(t)$  that maps  $\Omega$  diffeomorphically to the deformed state  $\Omega_t$  at time  $t$ . Since  $\varphi(\cdot, 0) = \mathbf{I}$ , it holds  $\det(D\varphi(t)) > 0$  for all  $t \geq 0$ .

At the heart of the Cosserat approach, the deformation tensor  $F := D\varphi$  is multiplicatively decomposed,

$$F = F_e F_p = R_e U_e F_p, \quad (5)$$

with  $F_e, F_p$  the elastic and plastic deformation tensors,  $U_e \in \text{GL}(\mathbb{R}^d)$  the stretching component, and

$$R_e \in \text{SO}(d) := \{R \in \text{GL}(\mathbb{R}^d) \mid \det(R) = 1, R^t R = \mathbf{I}\}$$

the micro-rotations. In (5),  $U_e$  need not be symmetric and positive definite, i.e. the decomposition  $F_e = R_e U_e$  is *not* the polar decomposition. By

$$K_e := R_e^t D_x R_e = (R_e^t \partial_x R_e, R_e^t \partial_y R_e, R_e^t \partial_z R_e) \quad (6)$$

the third-order (right) curvature tensor is denoted;  $f_{\text{ext}}(t), M_{\text{ext}}(t)$  designate the external volume force densities and external volume couples applied to the crystal body;  $\sigma_Y > 0$  is the yield stress.

In (1), it is assumed that plastic deformations occur along  $I_p \geq 1$  a-priori given material-dependent single-slip systems, only. These slip systems are specified by tensors  $m_a \otimes n_a$ , where  $m_a$  denotes the slip vector and  $n_a$  the slip normal of slip system  $a$ ,  $1 \leq a \leq I_p$ . These vectors satisfy  $|m_a| = |n_a| = 1$  and  $m_a \cdot n_a = 0$ .

For  $\gamma = (\gamma_a)_{1 \leq a \leq I_p} \in \mathbb{R}^{I_p}$ , it is set

$$F_p = F_p(\gamma) := \mathbf{I} + \sum_{a=1}^{I_p} \gamma_a m_a \otimes n_a. \quad (7)$$

This formula is derived by integration from the rate form. For other time integrators, see [65]. As a result of plastic deformation, due to structural changes within the material like the increase of immobilized dislocations inside the crystal structure, hardening occurs, [14, 8]. By the infinite latent-hardening assumption, [12], it is sufficient to consider only one active slip system at at time. Numerically, the algorithm selects the first slip

system which is active. In the model,  $\kappa \in \mathbb{R}^{I_p}$  is a set of hardening parameters. In (1), the simple ansatz for the energy of stored dislocations, [6],  $V(\kappa) := \rho \left( \sum_{a=1}^{I_p} \kappa_a \right)^2$  with a constant  $\rho > 0$  has been used.

By  $W_{\text{st}}$  the stretching part of the mechanical stored energy density is denoted,  $W_c$  is the curvature part due to (micro-)rotations. The last two functionals are defined by, cf. [47, 6],

$$W_{\text{st}}(U_e) := \mu \|\text{sym } U_e - \mathbf{I}\|^2 + \mu_c \|\text{skw}(U_e - \mathbf{I})\|^2 + \frac{\lambda}{2} |\text{tr}(U_e - \mathbf{I})|^2, \quad (8)$$

$$W_c(K_e) := \mu_2 \|K_e\|^2 := \mu_2 \|D_x R_e\|^2 = \mu_2 \sum_{k=1}^3 \|\partial_{x_k} R_e\|^2. \quad (9)$$

In these formulas,  $\mu_2 := \frac{\mu}{2} L_c^2$ , where  $L_c > 0$  is an internal length scale and  $\mu > 0$ ,  $\lambda > 0$  are Lamé parameters,  $\mu_c \geq 0$  is the Cosserat couple modulus. Eqn. (9) is a special case of the general form

$$W_c(K_e) := \mu \frac{L_c^{1+p}}{2} (1 + \alpha_4 L_c^q \|K_e\|^q) (\alpha_5 \|\text{sym } K_e\|^2 + \alpha_6 \|\text{skw } K_e\|^2 + \alpha_7 |\text{tr}(K_e)|^2)^{\frac{1+p}{2}}$$

after setting  $\alpha_4 := 0$ ,  $\alpha_5 = \alpha_6 := 1$ ,  $\alpha_7 := 0$ , and  $p := 1$ . In (8),  $\text{sym } A := \frac{1}{2}(A + A^t)$ ,  $\text{skw } A := \frac{1}{2}(A - A^t)$  denote the symmetric and skew-symmetric part of a tensor  $A$ , respectively, and  $\text{tr}(A) := \sum_i A_{ii}$  is the trace operator,  $\|A\| := \sqrt{\text{tr}(A^t A)}$  the Frobenius matrix norm. As usual,  $\cdot$  is the inner product in  $\mathbb{R}^d$ ,  $\mathbf{u} \cdot \mathbf{v} := \sum_{i=1}^d u_i v_i$ . For  $A, B \in \mathbb{R}^{d \times d}$ ,  $A : B := \text{tr}(A^t B) = \sum_{i,j=1}^d A_{ij} B_{ij}$  denotes the inner product in  $\mathbb{R}^{d \times d}$ . For a general introduction to tensor calculus in plasticity see, e.g., [34, 40].

Eqn. (1) introduces a family of time-discrete minimization problems. The concept goes back to [52] and permits the application of the calculus of variations to plasticity. For a fixed discrete time step  $h > 0$  and known  $(\gamma^0, \kappa^0)$  at time  $t$ , the new  $(\varphi, R_e, \gamma)$  representing values at time  $t + h$  are calculated from (1). Finally,

$$\kappa_a := \kappa_a^0 - |\gamma_a - \gamma_a^0|, \quad 1 \leq a \leq I_p \quad (10)$$

is set and  $(\gamma, \kappa)$  become the initial values of the next time step.

Starting from a material free of dislocations,  $\kappa(\cdot, 0) = 0$ , as a consequence of the hardening law (10),  $\sum_{a=1}^{I_p} \kappa_a(t+h) \leq \sum_{a=1}^{I_p} \kappa_a(t) \leq 0$  for all times  $t$ . Therefore,  $-2\rho \sum_{a=1}^{I_p} \kappa_a^0 \geq 0$  in (1) specifies the increase of the yield stress  $\sigma_Y$  due to stored dislocations.

### 3 Numerical solution method

For the rest of this article,  $\Omega \subset \mathbb{R}^3$ , i.e.  $d = 3$ . When selecting a numerical solution scheme for (1), the first fundamental observation is that due to the presence of the non-local term  $W_c(K_e) \sim \|D_x R_e\|^2$  in  $\mathcal{E}$ , the minimization cannot be carried out for each discretization point separately. As now  $R_e$  needs to be computed, the optimization step of the Cosserat model is more memory-demanding than the previous numerical approaches [41, 31, 37]. Secondly, it is not possible to reformulate (1) and use  $F = D\varphi$  directly instead of  $\varphi$  as an argument of  $\mathcal{E}$ , since the condition  $\text{curl}(F) = 0$  may be violated, i.e. the computed  $F$  need not be a gradient.

Following the ideas in [7], for the computation and storage of  $R_e \in \text{SO}(3)$ , a non-unique parametrization by Euler angles is used.

For  $\alpha = (\alpha_1, \alpha_2, \alpha_3) \in \mathbb{R}^3$ , letting  $s_k := \sin(\alpha_k)$ ,  $c_k := \cos(\alpha_k)$  for  $k = 1, 2, 3$ ,

$$R_e(\alpha) := Q_3(\alpha_3) Q_2(\alpha_2) Q_1(\alpha_1) \quad (11)$$

$$\begin{aligned} &:= \begin{pmatrix} 1 & 0 & 0 \\ 0 & \cos \alpha_3 & \sin \alpha_3 \\ 0 & -\sin \alpha_3 & \cos \alpha_3 \end{pmatrix} \begin{pmatrix} \cos \alpha_2 & 0 & -\sin \alpha_2 \\ 0 & 1 & 0 \\ \sin \alpha_2 & 0 & \cos \alpha_2 \end{pmatrix} \begin{pmatrix} \cos \alpha_1 & \sin \alpha_1 & 0 \\ -\sin \alpha_1 & \cos \alpha_1 & 0 \\ 0 & 0 & 1 \end{pmatrix} \\ &= \begin{pmatrix} c_1 c_2 & s_1 c_2 & -s_2 \\ c_1 s_2 s_3 - s_1 c_3 & c_1 c_3 + s_1 s_2 s_3 & c_2 s_3 \\ s_1 s_3 + c_1 s_2 c_3 & s_1 s_2 c_3 - c_1 s_3 & c_2 c_3 \end{pmatrix}. \end{aligned} \quad (12)$$

The right hand side of (11) defines a rotation for any argument  $\alpha \in \mathbb{R}^3$  and the mapping  $\alpha \mapsto R_e(\alpha) \in \text{SO}(3)$  is onto. Eqn. (11) does not prefer one of the three spatial coordinates and, in contrast to other parameterizations

by Euler angles where two elementary rotations  $Q_k$  are along the same coordinate axis, implies, see [7] for a detailed derivation,

$$W_c(K_e(\alpha)) = 2 \frac{\mu}{2} L_c^2 \left( |\nabla \alpha_1|_2^2 + |\nabla \alpha_2|_2^2 + |\nabla \alpha_3|_2^2 \right) =: 2\mu_2 |\nabla \alpha|_2^2. \quad (13)$$

Here, the Euclidean norm  $|x|_2 := (\sum_{k=1}^3 x_k^2)^{\frac{1}{2}}$  in  $\mathbb{R}^3$  has been introduced. Of course, computing spatial derivatives of  $\alpha$  by (13) is faster than computing derivatives of  $R_e$ . In addition, the introduction of  $\alpha$  automatically ensures  $R = R_e(\alpha) \in \text{SO}(3)$  and helps to interpret the numerical results.

For the minimization of  $\mathcal{E}$ , it is desirable to apply Newton's method, but clearly,  $|\cdot|$  in (1) is not differentiable at the origin. To overcome this obstacle, for chosen small  $\varepsilon > 0$ , the modulus  $|x|$  is replaced by

$$r_\varepsilon(x) := \begin{cases} x, & x > \varepsilon, \\ x^2/\varepsilon, & -\varepsilon \leq x \leq +\varepsilon, \\ -x, & x < -\varepsilon. \end{cases} \quad (14)$$

With (14), (11) and (13), the minimization (1) becomes

$$\begin{aligned} \mathcal{E}_\varepsilon(\varphi, \alpha, \gamma) = & \int_{\Omega} \left[ W_{\text{st}}(R_e^t(\alpha) D\varphi F_p(\gamma)^{-1}) + 2\mu_2 |\nabla \alpha|_2^2 - f_{\text{ext}} \cdot \varphi - M_{\text{ext}} : R_e(\alpha) \right. \\ & \left. + \rho \left( \sum_{a=1}^{I_p} r_\varepsilon(\gamma_a - \gamma_a^0) \right)^2 + \sum_{a=1}^{I_p} r_\varepsilon(\gamma_a - \gamma_a^0) \left( \sigma_Y - 2\rho \sum_{a=1}^{I_p} \kappa_a^0 \right) \right] dx \rightarrow \min \end{aligned} \quad (15)$$

subject to the boundary conditions

$$\varphi = g_D, \quad \alpha = \alpha_D \quad \text{on } \partial\Omega \quad (16)$$

with  $\alpha_D$  such that  $R_e(\alpha_D) = R_D$ .

The spatial discretization of (15) is based on finite differences with equidistant spacing in each direction. For simplicity, let  $\Omega = (0, L_1) \times (0, L_2) \times (0, L_3)$ , and  $d_k \in \mathbb{N}$  be the number of discretization points in direction  $x_k$ ,  $k = 1, 2, 3$ . For mesh points

$$(y_{ijk})_{0 \leq i \leq d_1, 0 \leq j \leq d_2, 0 \leq k \leq d_3} := (i\eta_1, j\eta_2, k\eta_3)_{ijk} \in \overline{\Omega} \quad (17)$$

with equal spacings

$$\eta_1 := \frac{L_1}{d_1}, \quad \eta_2 := \frac{L_2}{d_2}, \quad \eta_3 := \frac{L_3}{d_3}, \quad (18)$$

the integral is approximated by the Newton–Cotes formula ( $\mathbf{d}$  notifies the dependence on  $(d_1, d_2, d_3)$ )

$$\mathcal{E}_\varepsilon(\varphi, \alpha, \gamma) = \int_{\Omega} e_\varepsilon(x) dx \approx E_\varepsilon^{\mathbf{d}} := \frac{\eta_1 \eta_2 \eta_3}{8} \sum_{i=0}^{d_1} \sum_{j=0}^{d_2} \sum_{k=0}^{d_3} N_{ijk} e_\varepsilon(y_{ijk}) \quad (19)$$

which is exact up to second order and where the weights in 3D are given by

$$N_{ijk} = \begin{cases} 1, & \text{if } y_{ijk} \text{ is a corner of } \overline{\Omega}, \\ 2, & \text{if } y_{ijk} \text{ is at an edge of } \overline{\Omega}, \\ 4, & \text{if } y_{ijk} \text{ is on a face of } \overline{\Omega}, \\ 8, & \text{if } y_{ijk} \in \Omega. \end{cases} \quad (20)$$

On the right of (19), the integrand  $e_\varepsilon$  of  $\mathcal{E}_\varepsilon$  depends on  $(\varphi, \alpha, \gamma)$  evaluated at the nodes  $y_{ijk}$ . Combined, (19), (7) and (11) provide an approximation of  $\mathcal{E}_\varepsilon$  by a discrete functional  $E_\varepsilon^{\mathbf{d}} : X^{\mathbf{d}} \rightarrow \mathbb{R}$  for the space

$$X^{\mathbf{d}} := \left\{ (\varphi, \alpha, \gamma)(y_{ijk}) \mid 0 \leq i \leq d_1, 0 \leq j \leq d_2, 0 \leq k \leq d_3 \right\} \cong \mathbb{R}^D$$

with dimension

$$D := (6 + I_p)(d_1 + 1)(d_2 + 1)(d_3 + 1).$$

For the computation of  $\nabla\alpha$  in (13), central differences are used where feasible and one-sided difference quotients are employed near  $\partial\Omega$ .

For the approximate numerical solution of (15), the regularity of  $E_\varepsilon^{\mathbf{d}}$  and the variational structure is exploited. A discrete solution to (15) is computed numerically with a Limited-Memory Broyden-Fletcher-Goldfarb-Shanno approach, [50]. The L-BFGS-algorithm is a quasi-Newton method where the Hessian is never computed or stored explicitly. Instead, only information from the past  $k$  steps is used to compute a rank-one approximation of the Hessian. For this update,  $4kD$  operations are required. The algorithm, [50, Algorithm 2], has thus a complexity of  $O(kD)$  where typically,  $k \leq 40$  for  $D = 10^4$ . Therefore, the L-BFGS method is a powerful tool for large problems. This method is combined with the inexact Moré-Thuente line searcher which satisfies the strong Wolfe conditions, see [45] for details.

A proof of convergence of the L-BFGS method is only known when the objective functional is twice continuously differentiable and convex, [50]. Here, the convexity of  $E_\varepsilon^{\mathbf{d}}$  fails (due to non-convexity in  $\varphi$ ), but the L-BFGS method converges nevertheless.

For the application of the L-BFGS method, it remains to compute

$$DE_\varepsilon^{\mathbf{d}}(\varphi, \alpha, \gamma) = \left( \frac{\partial E_\varepsilon^{\mathbf{d}}}{\partial \varphi}, \frac{\partial E_\varepsilon^{\mathbf{d}}}{\partial \alpha}, \frac{\partial E_\varepsilon^{\mathbf{d}}}{\partial \gamma} \right).$$

The results are summed up in the following lemma.

**Lemma 1** *Let  $W_{\text{st}}$  be given by (8),  $W_c$  be given by (9). Let  $0 \leq I \leq d_1$ ,  $0 \leq J \leq d_2$ ,  $0 \leq K \leq d_3$ ,  $1 \leq a \leq I_p$ ,  $1 \leq b \leq 3$  be fixed indices,*

$$N_{IJK}^\Gamma := \begin{cases} N_{IJK}, & \text{if } y_{IJK} \notin \partial\Omega, \\ 0, & \text{else.} \end{cases} \quad (21)$$

*Then, with  $S := R_e \left[ \mu(\text{sym } U_e - \mathbf{I}) + \mu_c \text{skw } U_e + \frac{\lambda}{2} \text{tr}(U_e - \mathbf{I}) \mathbf{I} \right] (F_p^{-1})^t$ , with  $T_a := U_e \frac{\partial F_p}{\partial \gamma_a} F_p^{-1}$ , and  $C_b := \frac{\partial (Q_1^t Q_2^t Q_3^t)}{\partial \alpha_b} F_e$ , it holds*

$$\begin{aligned} \frac{\partial E_\varepsilon^{\mathbf{d}}(\varphi, \alpha, \gamma)}{\partial \varphi_b^{IJK}} &= \frac{\eta_1 \eta_2 \eta_3}{8} \left\{ \frac{N_{I-1,J,K}^\Gamma}{\eta_1} S_{b1}(y_{I-1,J,K}) - \frac{N_{I+1,J,K}^\Gamma}{\eta_1} S_{b1}(y_{I+1,J,K}) \right. \\ &\quad + \frac{N_{I,J-1,K}^\Gamma}{\eta_2} S_{b2}(y_{I,J-1,K}) - \frac{N_{I,J+1,K}^\Gamma}{\eta_2} S_{b2}(y_{I,J+1,K}) \\ &\quad \left. + \frac{N_{I,J,K-1}^\Gamma}{\eta_3} S_{b3}(y_{I,J,K-1}) - \frac{N_{I,J,K+1}^\Gamma}{\eta_3} S_{b3}(y_{I,J,K+1}) - N_{IJK}^\Gamma f_{\text{extb}}(y_{IJK}) \right\}, \end{aligned} \quad (22)$$

$$\begin{aligned} \frac{\partial E_\varepsilon^{\mathbf{d}}(\varphi, \alpha, \gamma)}{\partial \alpha_b^{IJK}} &= \frac{\eta_1 \eta_2 \eta_3}{4} \left\{ \frac{\mu_2}{2} \left( \Sigma_{1,b}^{IJK}(\alpha) + \Sigma_{2,b}^{IJK}(\alpha) + \Sigma_{3,b}^{IJK}(\alpha) \right) - N_{IJK}^\Gamma M_{\text{ext}}(t)(y_{IJK}) : \frac{\partial (Q_3 Q_2 Q_1)(\alpha^{IJK})}{\partial \alpha_b^{IJK}} \right. \\ &\quad \left. + N_{IJK}^\Gamma \left[ \mu(\text{sym } U_e - \mathbf{I}) : \text{sym } C_b + \mu_c \text{skw } U_e : \text{skw } C_b + \frac{\lambda}{2} \text{tr}(U_e - \mathbf{I}) \text{tr}(C_b) \right] (y_{IJK}) \right\}, \end{aligned} \quad (23)$$

$$\begin{aligned} \frac{\partial E_\varepsilon^{\mathbf{d}}(\varphi, \alpha, \gamma)}{\partial \gamma_a^{IJK}} &= \frac{\eta_1 \eta_2 \eta_3}{8} N_{IJK} \left\{ \left[ \sigma_Y - V' \left( \kappa^0 - \sum_{e=1}^{I_p} r_\varepsilon(\gamma_e - \gamma_e^0) \right) \right] r'_\varepsilon(\gamma_a - \gamma_a^0) - 2\mu(\text{sym } U_e - \mathbf{I}) : \text{sym } T_a \right. \\ &\quad \left. - 2\mu_c \text{skw } U_e : \text{skw } T_a - \lambda \text{tr}(U_e - \mathbf{I}) \text{tr}(T_a) \right\} (y_{IJK}). \end{aligned} \quad (24)$$

The symbols  $\Sigma_{1,b}^{IJK}$ ,  $\Sigma_{2,b}^{IJK}$ ,  $\Sigma_{3,b}^{IJK}$  in (23) originate from derivatives of the curvature energy and are defined by

$$\Sigma_{1,b}^{IJK}(\alpha) := \begin{cases} N_{I-1,J,K}^{\Gamma} \frac{\alpha_b^{IJK} - \alpha_b^{I-2,J,K}}{\eta_1^2} - N_{I+1,J,K}^{\Gamma} \frac{\alpha_b^{I+2,J,K} - \alpha_b^{IJK}}{\eta_1^2}, & 2 \leq I \leq d_1 - 2, \\ 4N_{0,J,K}^{\Gamma} \frac{\alpha_b^{1,J,K} - \alpha_b^{0,J,K}}{\eta_1^2} + N_{2,J,K}^{\Gamma} \frac{\alpha_b^{1,J,K} - \alpha_b^{3,J,K}}{\eta_1^2}, & I = 1, \\ N_{d_1-2,J,K}^{\Gamma} \frac{\alpha_b^{d_1-1,J,K} - \alpha_b^{d_1-3,J,K}}{\eta_1^2} + 4N_{d_1,J,K}^{\Gamma} \frac{\alpha_b^{d_1-1,J,K} - \alpha_b^{d_1,J,K}}{\eta_1^2}, & I = d_1 - 1, \\ 0, & I = 0 \text{ or } I = d_1, \end{cases}$$

$$\Sigma_{2,b}^{IJK}(\alpha) := \begin{cases} N_{I,J-1,K}^{\Gamma} \frac{\alpha_b^{IJK} - \alpha_b^{I,J-2,K}}{\eta_2^2} - N_{I,J+1,K}^{\Gamma} \frac{\alpha_b^{I,J+2,K} - \alpha_b^{IJK}}{\eta_2^2}, & 2 \leq J \leq d_2 - 2, \\ 4N_{I,0,K}^{\Gamma} \frac{\alpha_b^{I,1,K} - \alpha_b^{I,0,K}}{\eta_2^2} + N_{I,2,K}^{\Gamma} \frac{\alpha_b^{I,1,K} - \alpha_b^{I,3,K}}{\eta_2^2}, & J = 1, \\ N_{I,d_2-2,K}^{\Gamma} \frac{\alpha_b^{I,d_2-1,K} - \alpha_b^{I,d_2-3,K}}{\eta_2^2} + 4N_{I,d_2,K}^{\Gamma} \frac{\alpha_b^{I,d_2-1,K} - \alpha_b^{I,d_2,K}}{\eta_2^2}, & J = d_2 - 1, \\ 0, & J = 0 \text{ or } J = d_2, \end{cases}$$

$$\Sigma_{3,b}^{IJK}(\alpha) := \begin{cases} N_{I,J,K-1}^{\Gamma} \frac{\alpha_b^{IJK} - \alpha_b^{I,J,K-2}}{\eta_3^2} - N_{I,J,K+1}^{\Gamma} \frac{\alpha_b^{I,J,K+2} - \alpha_b^{IJK}}{\eta_3^2}, & 2 \leq K \leq d_3 - 2, \\ 4N_{I,J,0}^{\Gamma} \frac{\alpha_b^{I,J,1} - \alpha_b^{I,J,0}}{\eta_3^2} + N_{I,J,2}^{\Gamma} \frac{\alpha_b^{I,J,1} - \alpha_b^{I,J,3}}{\eta_3^2}, & K = 1, \\ N_{I,J,d_3-2}^{\Gamma} \frac{\alpha_b^{I,J,d_3-1} - \alpha_b^{I,J,d_3-3}}{\eta_3^2} + 4N_{I,J,d_3}^{\Gamma} \frac{\alpha_b^{I,J,d_3-1} - \alpha_b^{I,J,d_3}}{\eta_3^2}, & K = d_3 - 1, \\ 0, & K = 0 \text{ or } K = d_3. \end{cases}$$

Due to the boundary conditions (16) on  $\varphi$  and  $\alpha$ , the equations (22) and (23) are only evaluated for  $1 \leq I \leq d_1 - 1$ ,  $1 \leq J \leq d_2 - 1$ ,  $1 \leq K \leq d_3 - 1$ , i.e. the right hand sides of (22), (23) are well-defined.

**Proof.** The equations (22)–(24) are obtained by direct calculations starting from (15) and (19), using the chain rule and  $\frac{\partial(F_p^{-1})}{\partial\gamma_a} = -F_p^{-1} \frac{\partial F_p}{\partial\gamma_a} F_p^{-1}$ .  $\square$

Similarly,  $E_\varepsilon^d \in C^2(X^d; \mathbb{R})$  can be shown, an essential requirement of the convergence analysis in [50].

**Remark 1** Each component  $\alpha_k$  of  $\alpha$  is a solution of a scalar Allen-Cahn equation, [7], which is known to respect the maximum principle, see [26, 54] for a proof. Consequently, for all  $x \in \Omega$ ,

$$\min_{\partial\Omega} \alpha_{D,k} \leq \alpha_k(x) \leq \max_{\partial\Omega} \alpha_{D,k}, \quad k = 1, 2, 3.$$

Remark 1 also explains why the algorithm does not require a projection step (e.g. to the interval  $[0, 2\pi)$ ) of the computed  $\alpha_k$ .

#### 4 Numerical simulations

In Section 4.1 a benchmark problem is studied and the convergence behavior of the algorithm is worked out. Then, 3D bending experiments are simulated. The final section deals with the torsion of a rod.

All computations are dimensionless. The computations of the first section 4.1 share the parameters

$$\begin{aligned} \Omega &= (0, 1)^3, t \in [0, 1], \beta(t) = 0.25 * t, h = 0.1, \varepsilon = 10^{-4}, I_p = 1, \\ m_1 &= (1, 0, 0)^t, n_1 = (0, 1, 0)^t, \rho = \sigma_Y = 0, f_{\text{ext}} = 0, M_{\text{ext}} = \mathbf{0}. \end{aligned} \tag{25}$$

#### 4.1 A benchmark problem

In [7], a class of analytic solutions to a Cosserat medium in 3D is computed analytically assuming (7) and

$$D\varphi(t) = \mathbf{I} + \sum_{a=1}^{I_p} \beta_a(t) m_a \otimes n_a \quad \text{on } \partial\Omega \quad (26)$$

where  $\beta(t) = (\beta_1(t), \dots, \beta_{I_p}(t))$  is the prescribed shear. Subsequently, for the case of an ultra-soft material, i.e. for  $\sigma_y = \rho = 0$ , this problem is used as a benchmark. The numerical tests recover the analytic solution. In particular, (26) holds in  $\overline{\Omega}$ , i.e. the Cauchy-Born rule holds.

**Simulation 1:**  $\lambda = 10^3$ ,  $\mu = 10^4$ ,  $\mu_c = 2 \cdot 10^4$ ,  $\mu_2 := \mu \frac{L_c^2}{2} = 100$ .

*Initial values:*  $\varphi_0 \equiv \mathbf{I}$ ,  $\kappa^0 = \gamma^0 \equiv 0$  in  $\Omega$ .

*Boundary conditions* at  $\partial\Omega$ :  $\varphi(x, t) = (x_1 + \beta(t)x_2, x_2, x_3)$ ,  $\alpha \equiv 0$  at  $\partial\Omega$ .

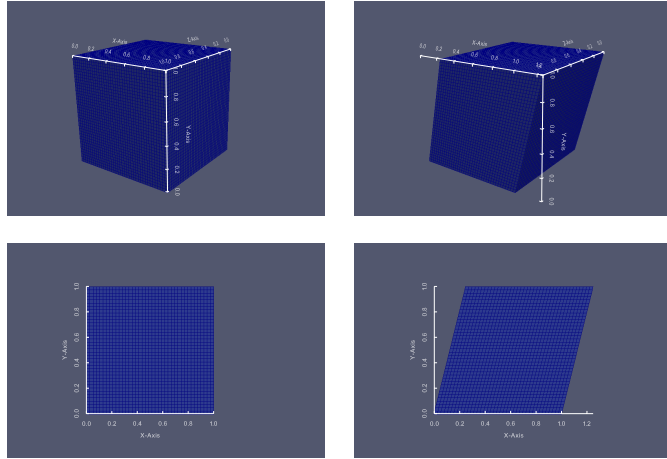


**Fig. 1** Computed shear of  $\Omega = (0, 1)^3$  along  $(1, 0, 0) \otimes (0, 1, 0)$ ,  $d_1 = d_2 = d_3 = 40$ . Left: undeformed material. Right: deformed solid at  $t = 1$ .

**Results:**  $\gamma(\cdot, t) \equiv \beta(t)$ ,  $R_e = U_e \equiv \mathbf{I}$ ,  $W_{st} = W_c \equiv 0$  in  $\overline{\Omega}$ ,  
 $\varphi(x, t) = (x_1 + \beta(t)x_2, x_2, x_3)$  in  $\Omega$ , i.e. the validity of Eqn. (26).

$(d_1, d_2, d_3)$	no. nodes	no. unknowns	time ( $\delta = 10^{-5}$ )	time ( $\delta = 10^{-6}$ )
$10 \times 10 \times 10$	1000	4072	0.94 s	1.1 s
$20 \times 20 \times 20$	8000	42992	30.4 s	39.6 s
$30 \times 30 \times 30$	27000	158712	211.2 s	291.2 s
$40 \times 40 \times 40$	64000	393232	732 s	1052 s
$50 \times 50 \times 50$	125000	788552	1508 s	2928 s
$60 \times 60 \times 60$	216000	1386672	2762 s	6100 s
$70 \times 70 \times 70$	343000	2229592	5674 s	11777 s

**Table 1** Comparison of the first time step for the benchmark problem, different spatial resolutions and the two chosen relative precisions  $E_e^d < \delta$  for  $\delta = 10^{-5}$  and  $\delta = 10^{-6}$ . The tabulated times are the computation times of the L-BFGS algorithm and refer to one single desktop PC with Intel Dual-Core E7400 (2.8GHz) and 4GB RAM.

$(d_1, d_2, d_3)$	$\delta = 10^{-5}$	$\delta = 10^{-6}$	$\delta = 10^{-7}$	$\delta = 10^{-8}$	$\delta = 10^{-10}$
$10 \times 10 \times 10$	460	552	635	689	804
$20 \times 20 \times 20$	1393	1795	2177	2606	3308
$30 \times 30 \times 30$	2517	3489	4366	5290	7330
$40 \times 40 \times 40$	3335	4805	6824	9068	12730
$50 \times 50 \times 50$	3445	6387	9844	13289	19787
$60 \times 60 \times 60$	3521	7814	12471	17584	27795
$70 \times 70 \times 70$	4057	9244	14857	22219	35517

**Table 2** L-BFGS iterations required to satisfy  $E_\epsilon^d < \delta$  for the first time step of the benchmark problem, different spatial resolutions and different relative precisions  $\delta$ .

Table 1 gives an overview of the computation times of the code and the number of unknowns for different spatial resolutions. Table 2 displays the required L-BFGS iteration steps needed to obtain a desired accuracy  $E_\epsilon^d < \delta$  for different values of  $\delta$  and different spatial resolutions. Since  $\mathcal{E} = 0$  for the analytic solution,  $E_\epsilon^d$  also measures the total numerical error. In order to have a meaningful test, no knowledge about the converged solution is used when picking the start values of the L-BFGS iteration. For the data of Table 1, Table 2 and Fig. 1, randomly  $\alpha \in [0, 2\pi)^3$  in  $\Omega$  is chosen as start values.

The boundedness of  $\mathcal{E}$  implies the boundedness of  $W_c(K_e) \sim \mu_2 \|D_x R_e\|^2$ . Due to the Rellich-Kondrakov theorem, this term is essential for the existence of minimizers as it provides compactness for sequences of  $R_e$ . Eqn. (13) converts this into a compactness property for  $\alpha$ . Correspondingly,  $2\mu_2 |\nabla \alpha|_2^2$  stabilizes the numerical scheme as it damps oscillations in  $\alpha$ . Clearly, the smaller  $\mu_2$ , the weaker this effect. Fig. 2 below documents this feature showing that the required L-BFGS iterations increase for smaller values of  $\mu_2$ .

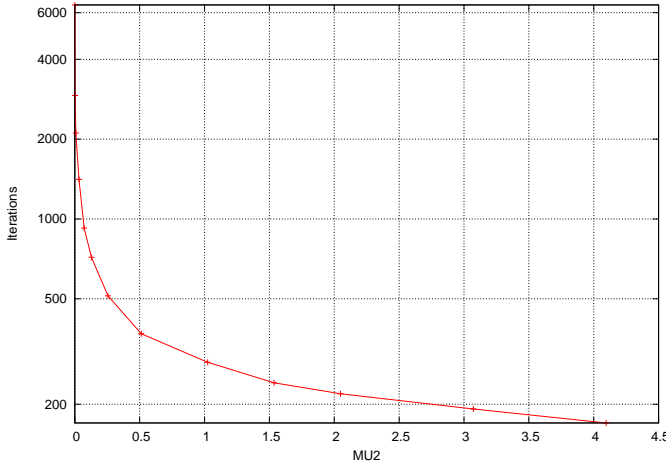


**Fig. 2** Number of L-BFGS iterations for the first time step of Simulation 1 and different values of  $\mu_2$ . Only  $\mu_2$  is varied, the other parameters are kept fixed with the values stated for Simulation 1.

#### 4.2 A 3D bending experiment

While the previous subsections focused on the characteristics of the algorithm itself, in this section a bending experiment for a rod is simulated. The parameters of the simulation are as in (25), but with

$$\Omega = (0, L_1) \times (0, L_2) \times (0, L_3) := (0, 5) \times (0, 1) \times (0, 2).$$

For given  $\beta(t)$ , the deformation at  $\partial\Omega$  is prescribed by

$$\varphi(x_1, x_2, x_3, t) := \left( x_2 + \frac{2L_1}{\pi} \left[ \sin \left( \frac{x_1}{2} + \frac{\pi}{2} \frac{x_1}{L_1} \right) + 1 \right] \beta(t) \right). \quad (27)$$

The implementation of the singular value decomposition for solving (4) uses the algorithm in [17] based on the Householder transformation. In tests, this method turned out more robust than the algorithm in [68]. After  $R_D$  has been computed by (4), in the last step  $\alpha_D$  is determined such that  $R_e(\alpha_D) = R_D$ . This is done with the algorithm in [60].

**Simulation 2:**  $\lambda = \mu = 0.025$ ,  $\mu_c = 0.4$ ,  $\mu_2 = 0.02$ . Other parameters are as in (25).

Spatial discretization:  $d_1 = 200$ ,  $d_2 = 40$ ,  $d_3 = 80$ .

Initial values:  $\varphi_0 \equiv \mathbf{I}$ ,  $\kappa^0 = \gamma^0 \equiv 0$  in  $\Omega$ .

Boundary conditions at  $\partial\Omega$ :  $\varphi(x, t)$  given by (27),  $\alpha = \alpha_D$  with  $R_e(\alpha_D) = R_D$  given by (3).

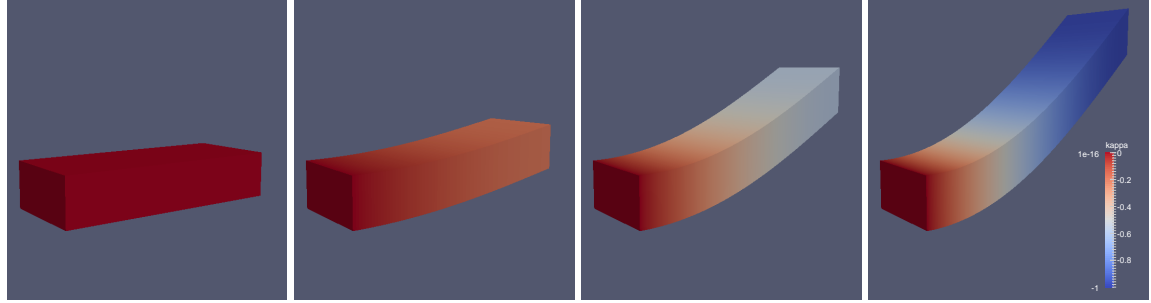


**Fig. 3** Spatial distribution of  $\kappa$  for Simulation 2 and  $t = 0.0$ ,  $t = 0.03$ ,  $t = 0.07$ ,  $t = 0.1$ .

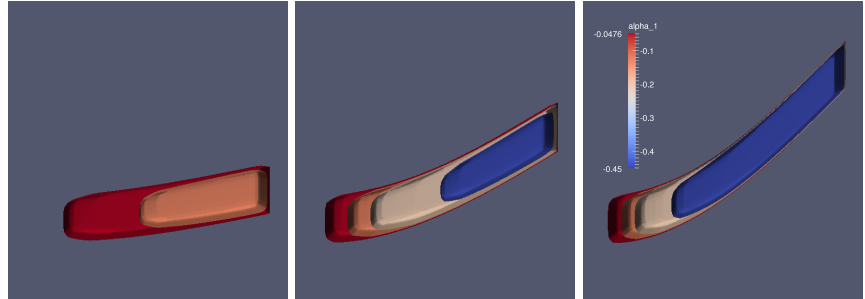


**Fig. 4** Level sets of  $\alpha_1$  at  $t = 0.03$ ,  $t = 0.07$ ,  $t = 0.1$  for Simulation 2.

**Results:**  $\alpha_2 = \alpha_3 \equiv 0$ ,  $\gamma(x, t) = \sin(\frac{\pi x_1}{2 L_1})\beta(t)$ ,  $U_e = \mathbf{I}$ ,  $W_{st} \equiv 0$  in  $\overline{\Omega}$ ,  $\varphi(x, t)$  follows (27) for  $x \in \overline{\Omega}$ .

Fig. 3 and Fig. 4 display the spatial distribution of  $\kappa$  and  $\alpha_1$ . For  $t \in [0, 0.1]$ , the boundary conditions (3) impose a range  $[-0.38, +0.38]$  on  $\alpha_1$  and enforce  $\alpha_2 = \alpha_3 = 0$  on  $\partial\Omega$ , hence in  $\overline{\Omega}$  by Remark 1. Consequently, the local minimum of  $J(\alpha) = W_{st}(R_e(\alpha))$  at  $\alpha_1 = \pi$  is not reached and no deformation patterning occurs.

#### 4.3 The effect of the discrete lattice point group

This subsection studies the influence of the discrete point group on the formation of rotation deformation zones. To this end, an additional term  $\eta \text{ dist}(R_e(\alpha), \mathcal{R})$  is added to  $\mathcal{E}$  in (1) with  $\eta > 0$  a constant and  $\mathcal{R}$  the discrete point group of the material, owing to the fact that certain rotations are preferred by the crystal lattice. The mechanical energy  $\mathcal{E}$  with this modification possesses additional local minima. Numerically, the minimisation problem

$$\text{dist}(R_e(\alpha), \mathcal{R}) = \min \left\{ \|R_e(\alpha) - M\| \mid M \in \mathcal{R} \right\} \quad (28)$$

is solved by passing through the finitely many elements of  $\mathcal{R}$ , using once more the parametrisation (12). This also provides a formula for  $\frac{d}{d\alpha} \text{dist}(R_e(\alpha), \mathcal{R})$  required for the computation of  $DE_e^d$ .

The following simulation documents the effects. The parameters are as in Section 4.1, but with  $\varphi$  at  $\partial\Omega$  prescribed by

$$\varphi(x_1, x_2, x_3, t) := \begin{pmatrix} x_2 + \frac{2L_1}{\pi} \left[ \sin\left(\frac{3\pi}{2} + \frac{\pi}{2} \frac{x_1}{L_1}\right) + 1 \right] \beta(t) \\ x_3 + \frac{2L_1}{\pi} \left[ \sin\left(\frac{3\pi}{2} + \frac{\pi}{2} \frac{x_1}{L_1}\right) + 1 \right] \beta(t) \end{pmatrix}. \quad (29)$$

This represents bending along two directions. Furthermore,  $\eta = 1$  is set and  $\mathcal{R}$  is chosen as the FCC lattice

$$\mathcal{R} = \{R = R_e(\alpha_1, \alpha_2, \alpha_3) \mid \alpha_k \in \{0, \pi/2, \pi, 3\pi/2\}\}.$$

Fig. 5 shows the results. As can be seen, additional patterning inside the slab occurs which is only due to the energy contribution of the lattice point group, i.e. disappears for  $\eta = 0$ .

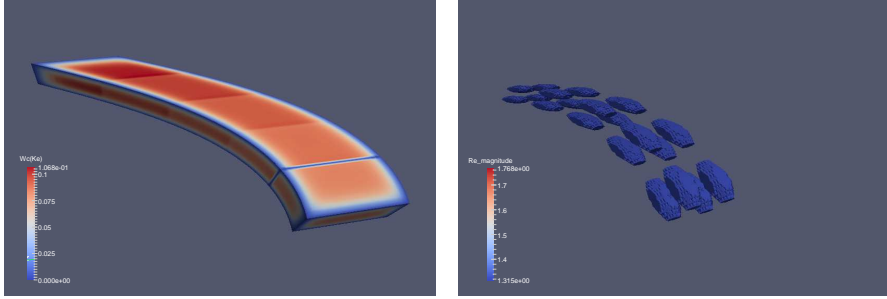


**Fig. 5** Bending of a slab with FCC lattice structure. Left: Curvature energy for the deformed slab at  $t = 0.05$ . Right: Additional patterning due to the energy contribution of the lattice point group.

#### 4.4 Torsion and stretching of a 3D rod

In the final computation, for given  $a(x_3, t)$ ,  $\beta(t)$ , the deformation at  $\partial\Omega$  is prescribed as

$$\varphi(x_1, x_2, x_3, t) := \begin{pmatrix} x_1 \cos(a(x_3, t)) - x_2 \sin(a(x_3, t)) \\ x_1 \sin(a(x_3, t)) + x_2 \cos(a(x_3, t)) \\ (1 + \beta(t))x_3 \end{pmatrix}. \quad (30)$$

This represents torsion of the material in the  $(x_1, x_2)$ -plane by an angle  $a(x_3, t)$  with simultaneous stretching by  $\beta(t)$ . The domain is chosen as a bar,  $\Omega = (0, 1) \times (0, 1) \times (0, 5)$ .

**Simulation 3:**  $\lambda = \mu = 0.025$ ,  $\mu_c = 0.4$ ,  $\mu_2 = 0.02$ ,  $\rho = \sigma_Y = 20$ ,  $a(x_3, t) := 4.0 * x_3 * t$ ,  $\beta(t) = 2.0 * t$ .

Other parameters as in (25). Spatial discretization:  $d_1 = d_2 = 20$ ,  $d_3 = 200$ .

*Initial values:*  $\varphi_0 \equiv \mathbf{I}$ ,  $\kappa^0 = \gamma^0 \equiv 0$  in  $\Omega$ .

*Boundary conditions at  $\partial\Omega$ :*  $\varphi(x, t)$  given by (30),  $\alpha = \alpha_D$  with  $R_e(\alpha_D) = R_D$  given by (3).

**Results:**  $\gamma(x, t) = \kappa(x, t) \equiv 0$ ,  $U_e = \mathbf{I}$ ,  $W_{st} \equiv 0$  in  $\overline{\Omega}$ ,  $\varphi(x, t)$  follows Eqn. (30) for  $x \in \overline{\Omega}$ .

$\alpha_3 \equiv 0$  in  $\overline{\Omega}$ .

The simulations show that the curvature energy is determined by the geometry of the slab. The stretching energy is largest near the top, and stretching leads to patterning of  $\alpha_1$  in  $x_3$ -direction. In contrast, patterning in  $\alpha_2$  is due to twisting and occurs perpendicular in the  $(x_1, x_2)$ -plane. Combined, the two effects lead to a complicated 3D-morphology. The computations also demonstrate how a length scale is introduced by  $\|\nabla R_e\|$ .

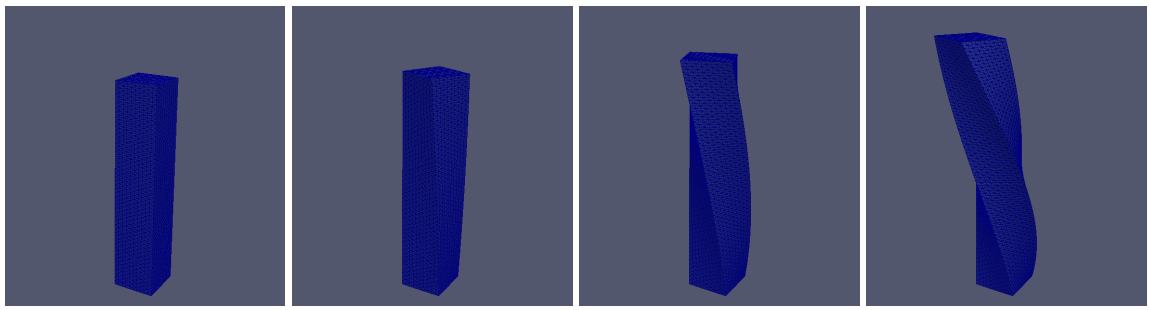


**Fig. 6** Twisting and stretching of the bar at  $t = 0.0$ ,  $t = 0.03$ ,  $t = 0.07$  and  $t = 0.1$ .

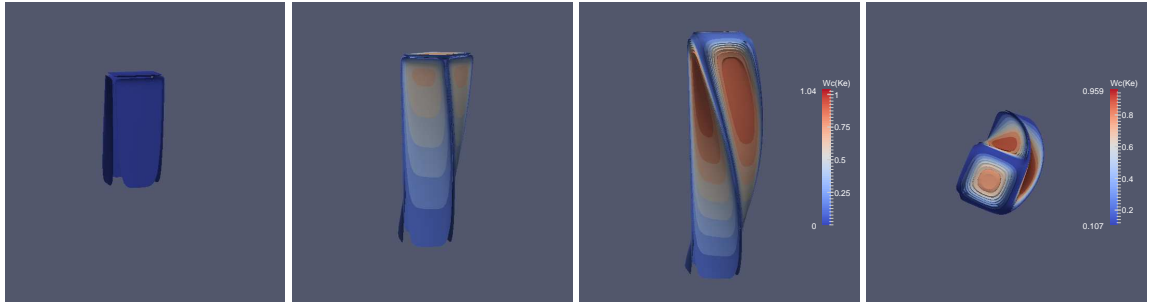


**Fig. 7** Iso-surfaces of the curvature energy at  $t = 0.03$ ,  $t = 0.07$ ,  $t = 0.1$ . Top view at  $t = 0.1$ .

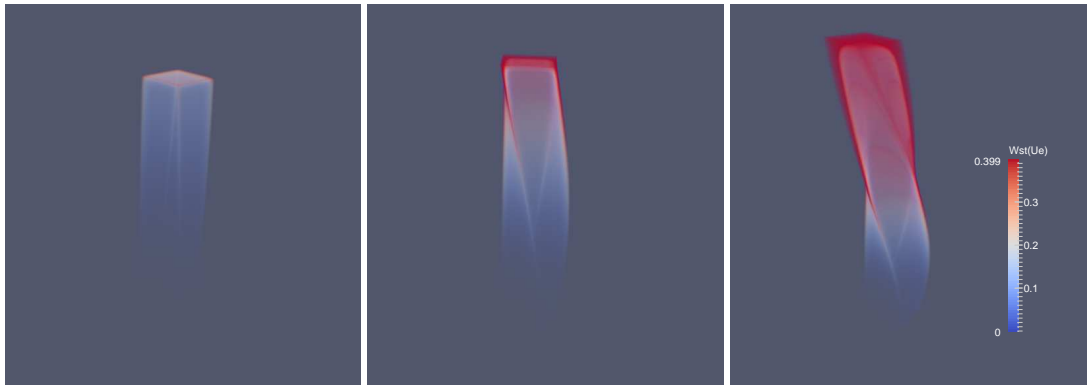


**Fig. 8** Volume plot of the stretching energy for  $t = 0.03$ ,  $t = 0.07$  and  $t = 0.1$ .

## 5 Discussion

In this article, a new algorithm for the solution of the finite-strain rate-independent Cosserat theory of crystal-plasticity was developed. A family of time-discrete minimization problems of the mechanical energy controlling the evolution of the material due to imposed deformations is solved with a variational ansatz, utilizing in 3D a limited-memory Broyden-Fletcher-Goldfarb algorithm based on finite differences.

In contrast to earlier algorithms, the method developed here does not rely on fictitious intermediate configurations and is capable of computing the micro-rotations, achieved by solving discrete systems with a larger number of unknowns. While the L-BFGS method does not store the Hessian and is thus specialized to such situations, see Table 1, some comments are in place regarding other aspects of the algorithm. Firstly, a disadvantage of introducing  $r_\varepsilon$  leading to (15) is that the onset of plasticity depends now on  $\varepsilon$  with more accurate predictions for smaller values of  $\varepsilon$ . On the other hand,  $r'_\varepsilon$  and thus  $D\varepsilon_\varepsilon$  explode for  $\varepsilon \searrow 0$ , resulting in numerical instabilities. Secondly, since  $SO(3)$  is a manifold, all charts are only locally invertible. Consequently, no representation of  $SO(3)$  works all the time and whether it is suitable or not depends on the studied problem. In case of the Euler angles (11), for every  $R \in SO(3)$  there exist two distinct  $\alpha^1, \alpha^2 \in [0, 2\pi]^3$

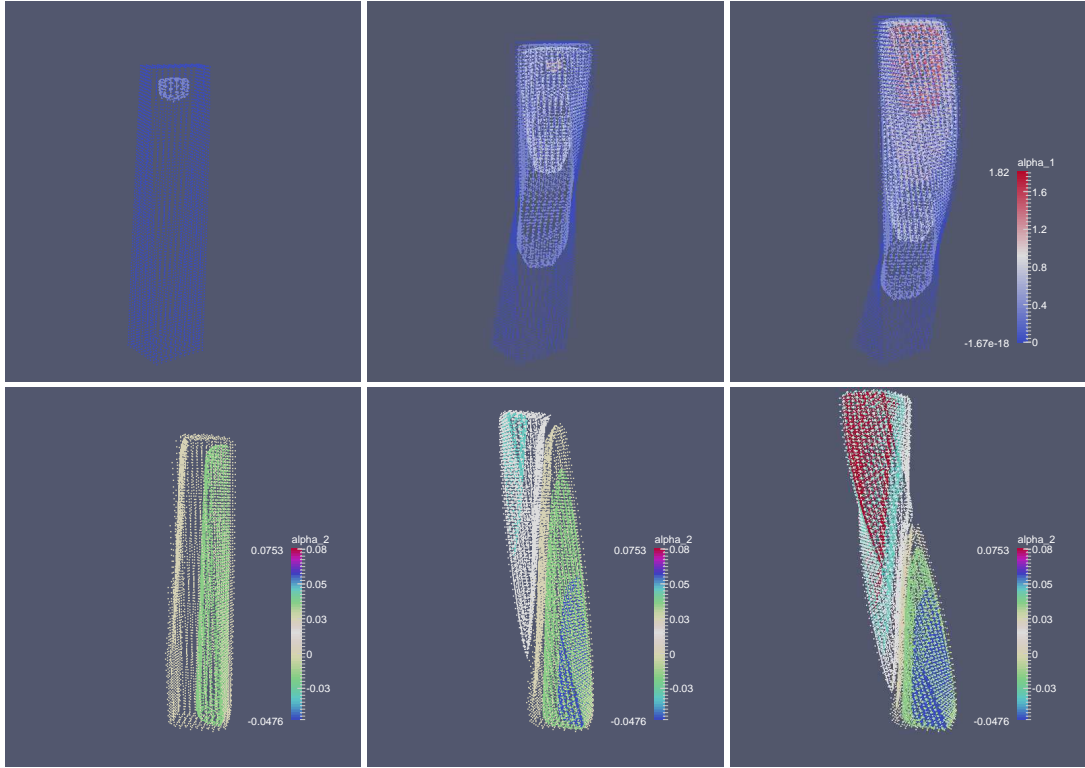


**Fig. 9** Spatial distribution of  $\alpha_1$  (top) and  $\alpha_2$  (bottom) for  $t = 0.03$  (left),  $t = 0.07$  (center) and  $t = 0.1$  (right).

with  $R_e(\alpha^1) = R_e(\alpha^2) = R$ . In certain cases, this non-uniqueness may lead to difficulties when the algorithm switches between the two local maps. A possible alternative to Euler angles are quaternions.

The investigated Cosserat model is very general and allows to study a large number of mechanical effects with a rich morphology. The present work is motivated by the analysis in [6, 7] where the occurrence of *deformation patterning* is predicted, i.e. the formation of cells in the material with approximately constant micro-rotations as a consequence of deformation, possibly leading to a better understanding why grains and subgrains form, [67, 27, 63, 51].

The computations carried out here are of principle nature. No attempt was made to adapt to particular materials. This would require quantum mechanical simulations, leading to energies which typically possess a large number of local minima. To some extend, the effect of such energies can already be studied at Fig. 5, where additional local minima of  $\mathcal{E}$  lead to increased deformation patterning. With regard to realistic simulations it must also be mentioned that the parameter identification is one of the major problems for the Cosserat model, [47].

**Acknowledgements** TB wishes to thank Prof. G. Gottstein and Prof. S. Luckhaus for valuable discussions.

## Appendix - List of symbols

$\Omega \subset \mathbb{R}^d$	reference domain, undeformed solid	$(x, t)$	space and time coordinates,
$\text{sym } \sigma$	symmetric part of tensor $\sigma$ , (8)	$\text{skw } \sigma$	skew-symmetric part of $\sigma$ , (8)
$\text{tr } \sigma$	trace of tensor $\sigma$	$\sigma^t$	transpose of $\sigma$ ; $R^t = R^{-1}$ for $R \in \text{SO}(3)$
$h > 0$	discrete time step	$\varepsilon > 0$	regularization of $ \cdot $ , (14)
$\varphi$	deformation vector of the solid, (5)	$F = D\varphi$	deformation tensor, (5)
$F_e$	elasticity tensor, (5)	$F_p$	plasticity tensor, (5)
$R_e$	rotation tensor, (5), (11)	$U_e$	(right) stretching tensor, (5)
$K_e$	(right) curvature tensor, (6)	$\mathbf{I}$	identity tensor, $(\mathbf{I})_{kl} = (\delta_{kl})_{kl}$
$\ \cdot\ $	Frobenius matrix norm, (8)	$\sigma_Y$	yield stress, (1)
$A : B$	tensor product of $A, B$ , below (9)	$\mathbf{u} \cdot \mathbf{v}$	inner product of $\mathbf{u}, \mathbf{v} \in \mathbb{R}^3$

$f_{\text{ext}}$	external volume forces, (1)	$M_{\text{ext}}$	external volume couples, (1)
$g_D$	Dirichlet boundary values of $\varphi$ , (2)	$R_D$	Dirichlet boundary values of $R_e$ , (2)
$W_{\text{st}}$	stretching energy, (8)	$W_c$	curvature energy, (9)
$I_p$	number of slip systems, (7)	$\rho > 0$	dislocation energy constant, (1)
$\lambda, \mu$	Lamé parameters, (8)	$\mu_c$	Cosserat couple modulus, (8)
$L_c$	internal length scale, (9)	$\mu_2$	parameter $\mu$ scaled by $L_c^2$ , (9)
$\gamma$	single-slip parametrization of $F_p$ , (7)	$\kappa$	dislocation density, (10)
$\gamma^0$	values of $\gamma$ at time $t$ , (10)	$\kappa^0$	values of $\kappa$ at time $t$ , (10)
$m_a$	slip vector of slip system $a$ , $1 \leq a \leq I_p$	$n_a$	slip normal of slip system $a$ , (7)
$\alpha$	Euler angle to $R_e$ in 3D, (11)	$\alpha_D$	Dirichlet boundary data of $\alpha$ , (16)
$A : B$	Tensor product of $A$ and $B$ , (9)	$ \cdot _2$	Euclidean vector norm in $\mathbb{R}^3$ , (13)
$L_1, L_2, L_3$	size of $\Omega$ , (18)	$d_{1,2,3}$	spatial resolution, (19)
$Q_i$	rotation along $x_i$ , (11)	$\beta(t)$	deformation parameter, (26), (27), (30)
$s_k$	$s_k = \sin(\alpha_k)$ , $1 \leq k \leq 3$ , (12)	$c_k$	$c_k = \cos(\alpha_k)$ , $1 \leq k \leq 3$ , (12)
$\mathcal{E}$	mechanical energy, (1)	$E_{\mathcal{E}}^d$	discretization of $\mathcal{E}$ , (19)
$y_{ijk}$	discretization points, (17)	$N_{IJK}^{(\Gamma)}$	discrete weights, (19), (20), (21)

## References

1. Aero, E.L., Bulygin, A.N., Kuvshinskii, E.V.: Asymmetric hydrodynamics, *Prikl. Mat. Mekh.* 29, 297–308 (1965)
2. Aero, E.L., Kuvshinskii, E.V.: Fundamental equations of the theory of elastic media with rotationally interacting particles, *Sov.Phys.Solid State* 2, 1272–1281 (1961)
3. Altenbach, H., Eremeyev, V.A., Lebedev, L.P. Rendón: Acceleration waves and ellipticity in thermoelastic micropolar media. *Archive of Applied Mechanics* 80, 217–227 (2010)
4. Allen, S.J., de Silva, C.N., Kline, K.A.: Theory of simple deformable directed fluids, *Phys. Fluids* 12, 2551–2555 (1967)
5. Altenbach, H., Eremeyev, V.A.: Generalized Continua from the Theory to Engineering Applications, Springer publishing, CISM, (2013)
6. Blesgen, T.: Deformation patterning in Cosserat plasticity. *Modelling Simulation Mater. Sci. Eng.* 21, (2013) DOI:10.1088/0965-0393/21/3/035001
7. Blesgen, T.: Deformation patterning in three-dimensional large-strain Cosserat plasticity, *Mechanics Research Communications* 62(C), 37–43 (2014) DOI 10.1016/j.mechrescom.2014.08.007
8. Blesgen, T., Luckhaus, S.: The Dynamics of Transition Layers in Solids with Discontinuous Chemical Potentials. *Math. Meth. Appl. Sciences* 29, 525–536 (2006)
9. de Borst, R., Sluys, L.J.: Localisation in a Cosserat continuum under static and dynamic loading conditions. *Computer Methods in Applied Mechanics and Engineering* 90, 805–827 (1991)
10. Capriz, G.: Continua with Microstructure, Springer publishing (1989)
11. Capriz, G., Giovine, P., Mariano P.M. (eds.): Mathematical models of granular matter, Lecture notes in Mathematics, Springer publishing (2008)
12. S. Conti, M. Ortiz: Dislocation Microstructures and the Effective Behavior of Single Crystals, *Arch. Rational Mech. Anal.* 176, 103–147
13. Cosserat, E., Cosserat, F.: Théorie des corps déformables, Librairie Scientifique A. Hermann et Fils, Paris (1909), (English version: Theory of deformable bodies, NASA TT F-11 561 (1968))
14. Crumbach, M., Goerdeler, M., Gottstein, G.: Modelling of recrystallisation textures in aluminium alloys: I. Model set-up and integration. *Acta Materialia* 54, 3275–3289 (2006)
15. de Silva, C.N., Tasi, P.J.: A general theory of directed surfaces, *Acta Mechanica* 18, 89–101 (1973)
16. Diebels, S.: A macroscopic description of the quasi-static behavior of granular materials based on the theory of porous media, *Granular Matter* 2, 143–152 (2000)
17. Dongarra, J.J., Bunch, J.R., Moler, C.B., Stewart, G.W.: LINPACK Users' Guide, SIAM, Philadelphia (1979)
18. V.A. Eremeyev, L.P. Lebedev, H. Altenbach: Foundations of Micropolar Mechanics, Springer (2013)
19. Erickson, J.L., Truesdell, C.: Exact theory of stress and strain in rods and shells, *Archive for Rational Mechanics and Analysis* 1, 295–323 (1958)
20. Eringen, A.C., Suhubi, E.S.: Nonlinear theory of simple micro-elastic solids. *Intern. Journal Eng. Sci.* 2, 189–203 (1964)
21. Eringen, A.C.: Linear theory of micropolar elasticity, *Journal of Mathematics and Mechanics* 15, 909–923 (1966)
22. Eringen, A.C.: Theory of thermomicrofluids, *Journal of Mathematical Analysis and Applications* 38, 480–496 (1972)
23. Eringen, A.C.: Theories of nonlocal plasticity. *Intern. Journal Eng. Sci.* 21, 741–751 (1983)
24. Eringen, A.C., Kafadar, C.B.: Polar field theories. In A.C. Eringen (Ed.): Continuum physics, polar and nonlocal field theories IV, Academic press, New York, 1–73 (1976)
25. Eringen, A.C.: A unified continuum theory of electrodynamics of liquid crystals, *International Journal of Engineering Science* 35, 1137–1157 (1997)
26. Evans, L.C., Soner, H.M., Souganidis, P.E.: Phase transitions and generalized motion by mean curvature. *Commun. Pure Appl. Math.* 45, 1097–1123 (1992)
27. Forest, S., Barbe, F., Cailletaud, G.: Cosserat modelling of size effects in the mechanical behaviour of polycrystals and multi-phase materials. *International Journal of Solids and Structures* 37, 7105–7126 (2000)
28. Forest, S., Sievert, R.: Elastoviscoplastic constitutive frameworks for generalized continua. *Acta Mech.* 160, 71–111 (2003)

29. Gomez, J.D.: Numerical treatment of cosserat based rate independent strain gradient plasticity theories. *Ingieria y Ciencia* 4, 99–128 (2008)
30. Gourgiotis, P.A., Georgiadis H.G.: Distributed dislocation approach for cracks in couple-stress elasticity: Shear Modes. *Int. J. Fract.* 147, 83–102 (2007)
31. Gammoudis, P., Tsakmakis C.: Predictions of microtorsional experiments by micropolar plasticity, *Proceedings of the Royal Society A* 461, 189–205 (2005)
32. Green A.E., Naghdi, P.M., Rivlin, R.S.: Directors and multipolar displacements in continuum mechanics, *International Journal of Engineering Sciences* 2, 611–620 (1965)
33. Günther, W.: Zur Statik und Kinematik des Cosseratschen Kontinuums. *Abhandlungen der Braunschweiger Wissenschaftlichen Gesellschaft Göttingen* 10, 196–213 (1958)
34. Han, W., Reddy, D.: Plasticity. Mathematical theory and numerical analysis, Springer publishing (1999)
35. Harris, D., Grekova, E.F.: A hyperbolic well-posed model for the flow of granular materials, *Journal of Engineering Mathematics* 52, 107–135 (2005)
36. Hill, R.: The mathematical theory of Plasticity. Oxford University Press, Oxford UK (1998)
37. Hirschberger C.B.: A treatise on micromorphic continua. Theory, Homogenization, Computation. PhD thesis, university of Kaiserslautern (2008)
38. Khoei, A.R., Yadegari, S., Biabanaki, S.O.R.: 3d finite element modeling of shear band localization via the micro-polar Cosserat continuum theory. *Comp. Mat. Science* 49, 720–733 (2010)
39. Kotera, H., Sawada, M., Shima, S.: Cosserat continuum theory to simulate microscopic rotation of magnetic powder in applied magnetic field, *International Journal of Mechanical Sciences* 42, 129–145 (2000)
40. Lubliner, J.: Plasticity Theory, Dover publications (2008)
41. Menzel, A., Ekh, M., Runesson, K., Steinmann, P.: A framework for multiplicative elastoplasticity with kinematic hardening coupled to anisotropic damage, *International Journal of Plasticity* 21, 397–434 (2005)
42. Maugin, G.A.: Mechanics of Generalized Continua – One hundred years after the Cosserats, Springer publishing 2010
43. Miehe, C.: A constitutive frame of elastoplasticity at large strains based on the notion of a plastic metric, *International Journal of Solids and Structures* 35 (30), 3859–3897 (1998)
44. Mindlin, R.D.: Micro-structure in linear elasticity. *Arch. Ration. Mech. Anal.* 16, 51–78 (1964)
45. Moré, J., Thuente, D.J.: Line search algorithms with guaranteed sufficient decrease, *ACM Transactions Math. Software* 20, 286–307 (2004)
46. Mugnai, L., Luckhaus, S.: On a mesoscopic many-body Hamiltonian describing elastic shears and dislocations, *Continuum Mechanics and Thermodynamics* 22, 251–290 (2010)
47. Neff, P.: A finite-strain elastic-plastic Cosserat theory for polycrystals with grain rotations. *Int. Journal of Eng. Science* 44, 574–594 (2006)
48. Neff, P., Chelminski, K.: Infinitesimal elastic-plastic Cosserat micropolar theory. Modelling and global existence in the rate-independent case. *Proc. Roy. Soc. Edinburgh A* 135, 1017–1039 (2005)
49. Neff, P., Chelminski, K., Müller, W., Wieners: A numerical solution method for an infinitesimal elasto-plastic Cosserat model. *Math. Models and Methods in Appl. Sciences* 17, 1211–1239 (2007)
50. Nocedal, J.: On the Limited Memory Method for Large Scale Optimization. *Math. Programming B* 45, 503–528 (1989)
51. Oda, M., Iwashita I. (Eds.): Mechanics of granular materials: an introduction. Taylor&Francis publishing (1999)
52. Ortiz, M., Repetto, E.: Nonconvex energy minimization and dislocation structures in ductile single crystals. *Journal. Mech. Phys. Solids* 47, 397–462 (1999)
53. Papanicopoulos, S.-A., Zervos, A.: A three-dimensional  $C^1$  finite element for gradient elasticity. *International Journal for Numerical Methods in Engineering* 77, 1396–1415 (2009)
54. Protter, M.H., Weinberger, H.F.: Maximum Principles in Differential Equations, Springer, New York (1999)
55. Reina, C., Conti, S.: Kinematic description of crystal plasticity in the finite kinematic framework: A micromechanical understanding of  $F = F_{\text{at}} F_{\text{p}}$ . *Journal of the Mechanics and Physics of Solids* 67, 40–61 (2014)
56. Rubin, M.B.: Cosserat theories: Shells, Rods and Points. Kluwer Academic Publishers, Dordrecht (2000)
57. Rubin, M.B.: Numerical solution of axisymmetric nonlinear elastic problems including shells using the theory of a Cosserat point, *Comput. Mech.* 36(4), 266288 (2005)
58. Simo, J.C.: A framework for finite strain elastoplasticity based on maximum plastic dissipation and the multiplicative decomposition, Part I: Continuum formulation. *Comp. Meth. Appl. Mech. Eng.* 66, 199–219 (1988)
59. Simo, J.C.: A framework for finite strain elastoplasticity based on maximum plastic dissipation and the multiplicative decomposition, Part II: Computational aspects. *Comp. Meth. Appl. Mech. Eng.* 68, 1–31 (1988)
60. Slabaugh, G.: Computing Euler angles from a rotation matrix. Technical report (1999). Available online at <http://www.soi.city.ac.uk/sbbh653/publications/euler.pdf>
61. Stojanovic, R. (ed.): Mechanics of polar continua, theory and applications, Springer publishing (1969)
62. Toupin, R.A.: Elastic materials with couple-stresses, *Archive for Rational Mechanics and Analysis* 17, 85–112 (1962)
63. Vardoulakis, I., Sulem, J.: Bifurcation analysis in geomechanics. Spon Press (1995)
64. Walsh, S.D.C., Tordesillas A.: A thermomechanical approach to the development of micropolar constitutive models of granular media, *Acta Mechanica* 167, 145–169 (2004)
65. Weber, G., Anand L.: Finite deformation constitutive equations and a time integration procedure for isotropic, hyperelastic-viscoplastic solids, *Comput. Methods Appl. Mech. Eng.* 79, 173–202 (1990)
66. Yeremeyev, V.A., Zubov, L.M.: The theory of elastic and viscoelastic micropolar liquids, *Journal of Applied Mathematics and Mechanics* 63, 755–767 (1999)
67. Zeghadi, A., Forest, S., Gourgues, A.-F., Bouaziz, O.: Cosserat continuum modelling of grain size effects in metal polycrystals. *Proc. Appl. Math. Mech.* 5, 79–82 (2005)
68. Zhang, H.W., Wang, H., Chen, B.S., Xie, Z.Q.: Analysis of Cosserat materials with Voronoi cell finite element method and parametric variational principle. *Comput. Methods Appl. Mech. Engrg.* 197, 741–755 (2008)
69. Zhilin, P.A.: Mechanics of deformable directed surfaces, *International Journal of Solids and Structures* 12, 635–648 (1976)